MODELING LOCAL FOULING RESISTANCES

F. Schlüter, W. Augustin and S. Scholl

Technische Universität Braunschweig, Institute for Chemical and Thermal Process Engineering,
Langer Kamp 7, 38106 Braunschweig, Germany
E-mail: f.schlueter@tu-braunschweig.de

ABSTRACT

Although fouling is a problem varying in space and time, a fouling situation is commonly quantified with the integral thermal fouling resistance based on the integral heat balance and an area-averaged heat transfer assessment. At the current status local differences like constrictions which affect the integral fluid dynamic behavior are not taken into consideration for modeling.

This work shows experimental and analytical results of local investigations of a fouled counterflow double-pipe heat exchanger. The determined local parameters are used to model local thermal and mass based fouling resistances as part of a holistic approach with the aim to link the thermal and the mass based approach. Therefore, mass based parameters are utilized to recalculate the obtained local thermal fouling resistances in order to account for the increase in heat transfer caused by local surface roughness and/or local constrictions. This approach aims to explain and eliminate apparent negative fouling resistances on a local basis.

For the determination of the local thermal fouling resistances local temperatures are measured to quantify the local overall heat transfer coefficients. For modeling local mass based fouling resistances the local material properties density and thermal conductivity are required. Furthermore, knowledge about the local layer thickness and/or the local fouling mass is needed. For recalculating local thermal fouling resistances local friction coefficients and local flow velocities resulting from the local constrictions are used. All experimental and theoretical approaches are merged into the model for the determination of local fouling resistances presented here.

INTRODUCTION

Fouling describes unwanted deposits on heat transfer surfaces and is a severe issue in the chemical and process industry. Therefore, fouling has been a subject to scientific investigations for decades (Müller-Steinhagen, 2011). One of the most prevalent deposition mechanism is crystallization fouling. The literature provides many works on the investigation and modeling of the time-dependent integral behavior of crystallization fouling regarding various scientific aspects (Bohnet and Augustin, 1993; Krause, 1993; Augustin and Bohnet, 1995; Helalizadeh et al., 2000; Müller-Steinhagen et al., 2000; Zettler et al., 2005; Al-Janabi et al., 2009; Pääkkönen et al., 2012), but only a few have been published on local investigations of crystallization fouling (Albert, 2010; Albert et al., 2011; Fahiminia et al., 2007; Goedecke et al., 2016; Schlüter et al., 2017).

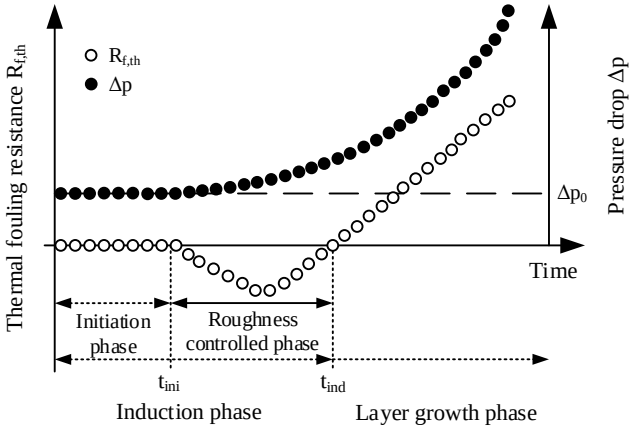

Fig. 1 Schematic development of the thermal fouling resistance and the pressure drop over process time; adapted from Schoenitz et al. (2015).

In accordance to Schoenitz et al. (2015) the progress of crystallization fouling typically comprises three consecutive phases as displayed in Fig. 1. The initiation phase is followed by the roughness controlled phase and the layer growth phase. The first two make up for the induction phase.

Fig. 2 schematically presents the progress of crystallization on a heat transfer surface. First crystals are formed on the surface during initiation phase, but initially with no noticeably influence on heat transfer (phase I). Phase IIa is part of the roughness controlled phase. With increasing crystal size and surface coverage the surface roughness leads to an enhanced heat transfer resulting in a negative thermal fouling resistance ultimately reaching a maximum. It is assumed that the roughness effect remains constant from this point on (Albert et al., 2011). Subsequently, single crystals cross-link and first fouling layers build up in clusters in direct contact to the heat transfer wall (IIb). Phase IIb is also a part of the roughness controlled phase and can be defined as a transition zone. The additional thermal resistance starts to override the heat transfer enhancement caused by roughness until the thermal fouling resistance becomes zero. Subsequently, phase IIb goes over into the actual layer

ISBN: 978-0-9984188-1-0; Published online www.heatexchanger-fouling.com

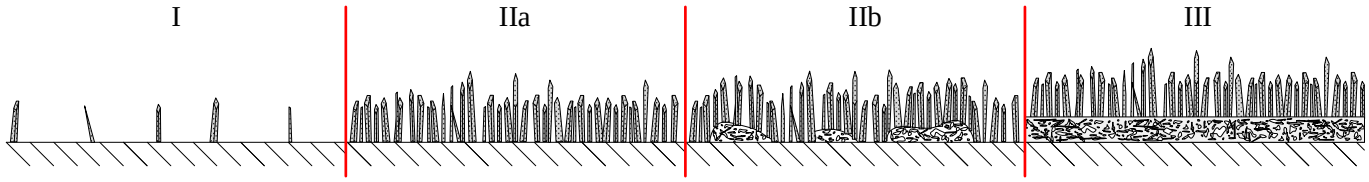

Fig. 2 Consecutive phases of crystallization on a heat transfer surface.

growth phase. Due to expansion the clusters connect to each other and a dense bottom layer is formed which covers the entire heat transfer surface in phase III. Consequently, the fouling resistance becomes positive due to increasing thermal resistance. In addition, the bottom layer grows with time and increasingly constricts the flow cross-section. In case of a constant flow rate the flow velocity increases caused by constriction. Hence, the heat transfer impeding effect of the growing fouling layer is superimposed by the simultaneous enhancement of the heat transfer due to fluid acceleration (Albert et al., 2011).

On the other hand roughness and constriction result in an increased pressure drop, already appearing in the induction phase, as shown in Fig. 1. Therefore, a distinction of the *fouling resistance* into a *thermal* and a *mass based* expression is required. A fundamental approach to model the integral fouling process was introduced in the 1950s by Kern and Seaton (1959) which was the basis for most of the fouling models developed afterwards (Müller-Steinhagen, 2011). The inlet and outlet temperatures of a heat exchanger quantify the change in the overall heat transfer resistance at soiled $\left(\frac{1}{k_f}\right)$ and clean $\left(\frac{1}{k_0}\right)$ state and determine the *integral thermal fouling resistance* $R_{f,th}$ according to Eq. (1).

$$R_{f,th}(t) = \frac{1}{k_f(t)} - \frac{1}{k_0} \tag{1}$$

The increasing pressure drop of a heat exchanger indicates the *integral mass based fouling resistance* $R_{f,mass}$ which is described with the deposited solid mass per unit area m_f as well as the density and thermal conductivity of the fouling layer.

$$m_f = \rho_f x_f \tag{2}$$

$$R_{f,mass}(t) = \frac{x_f(t)}{\lambda_f(t)} = \frac{m_f(t)}{\rho_f(t)\ \lambda_f(t)} \tag{3}$$

In order to eliminate apparent negative fouling values Albert et al. (2011) recalculated integral thermal fouling resistances by taking the heat transfer enhancing roughness and constriction effects into account:

$$R_{f,corr}(t) = \frac{1}{k_f(t)} - \frac{A}{\alpha_{i,0}\left(\varepsilon_{Nu,\xi}\varepsilon_{Nu,\omega}\right)_t A_i} - \left(\frac{x_w A}{\lambda_w A_m} + \frac{A}{\alpha_o A_o}\right) \tag{4}$$

The effect of increasing surface roughness on heat transfer is considered by extending the common integral fouling description with the factor $\varepsilon_{Nu,\xi}$ which defines the ratio of heat transfer due to friction of the rough surface Nu_ξ and heat transfer due to friction of the smooth surface Nu_0, see Eq.(5). For this purpose Albert et al. (2011) applied various heat transfer correlations accounting for surface roughness effects developed by Nunner (1956), Burck (1969), Hughmark (1975) and Ceylan and Kelbaliyev (2003).

$$\varepsilon_{Nu,\xi} = \frac{Nu_\xi}{Nu_0} \tag{5}$$

In addition, the constriction effect on heat transfer is considered by $\varepsilon_{Nu,\omega}$ which describes the ratio of the Nusselt numbers with and without constriction due to fouling. The increase in Nusselt number by acceleration effects can be determined with the well-known correlation of Gnielinski (1995) for turbulent pipe flow, see Eq. (7).

$$\varepsilon_{Nu,\omega} = \frac{Nu_\omega}{Nu_0} \tag{6}$$

$$Nu_\omega = \frac{\left(\xi/8\right)RePr}{1+12.7\sqrt{\xi/8}\left(Pr^{2/3}-1\right)}\left[1+\left(\frac{d_{i,f}(z)}{z}\right)^{2/3}\right] \tag{7}$$

The recalculated fouling curves obtained by using Eq. (4) and applying the approaches of Burck (1969) and Ceylan and Kelbaliyev (2003) started with a physically unacceptable offset and showed unrealistic high fouling resistances (Albert et al., 2011). More realistic results can be found by using the empirical correlations of Nunner (1956) and Hughmark (1975).

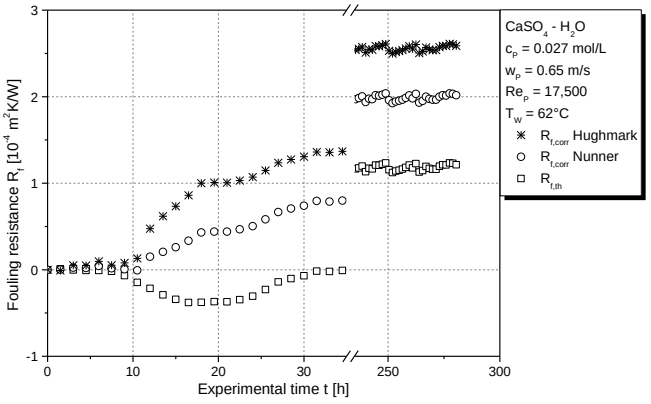

Fig. 3 Recalculated fouling resistances accounting for roughness and constriction effects on heat transfer; adapted from Albert et al. (2011).

ISBN: 978-0-9984188-1-0; Published online www.heatexchanger-fouling.com

Fig. 3 shows the corrected fouling resistances which are reasonable in comparison to the fouling resistance calculated with a constant heat transfer coefficient according to Eq. (1). The resulting fouling curves reach asymptotic resistances, which differ in their absolute values depending on the approach applied.

The studies from Albert (2010) and Goedecke et al. (2016) showed local differences of the thermal fouling resistance along the inner tube of a counterflow double-pipe heat exchanger with a length of 2 m. Both found that the integral assessment of the fouling process is not suitable to detect local processes or to identify the proceeding sub-processes and their interactions and to explain the determining mechanisms. Therefore, both a local and a time-resolved acquisition, analysis and modeling is essential for a deeper insight into the fouling process. Subsequently, the studies on local $CaSO_4$ fouling have been extended with various experimental investigations by Schlüter et al. (2017).

Continuing this work, experimental results will be used in this paper to calculate additionally necessary input data for modeling local thermal and local mass based fouling resistances based on Eqs. (1) and (3). Furthermore, the approach to recalculate integral thermal fouling resistances, see Eq. (4), will now be applied on local thermal fouling resistances, obtained experimentally, in order to link the thermal and mass based approach. An overview of the applied modeling approach is presented in the following section.

MODELING CONCEPT

This section introduces the core structure of a new holistic approach to model fouling resistances at first. The part of the model, this work deals with, is presented more detailed afterwards.

Core of the holistic fouling model

Fig. 4 shows the core structure of the holistic model. A distinction is made between local and integral thermal, local and integral mass based as well as corrected local and corrected integral fouling resistances. A direct correlation between local thermal fouling resistances, based on local temperature measurements, and the integral thermal fouling resistance, based on the integral heat balance, is not possible (Goedecke et al., 2016). Furthermore, thermal fouling resistances cannot be correlated directly with mass based fouling resistances. For this reason Albert et al. (2011) developed a model which corrects integral thermal fouling resistances by eliminating heat transfer enhancing roughness and constriction effects. The computation, processed integrally so far, will now be extended and integrated into a local consideration for recalculating local thermal fouling resistances. The future goal is to link the corrected fouling resistances with mass based fouling resistances as displayed with the broken lines in Fig. 4.

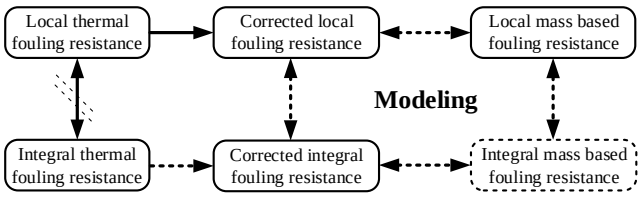

Fig. 4 Core structure of the comprehensive approach to model fouling resistances.

Local fouling resistances

Fig. 5 deals with the upper part of the holistic approach in Fig. 4 and shows the composition of modeling local fouling resistances in detail. Rectangles indicate measured data while calculated parameters are displayed in rectangles with rounded corners, finally leading to the three target boxes. The modeling of the three different fouling resistances is described briefly in the following. The experimental and theoretical approaches to obtain the required parameters in the respective boxes are presented afterwards.

Local thermal fouling resistance

For the determination of local thermal fouling resistances local temperatures measured at the wall and in the heating medium are utilized to quantify local overall heat transfer coefficients.

$$R_{f,th,loc} = \frac{1}{k_f(t,z)} - \frac{1}{k_0(z)} \tag{8}$$

Corrected local fouling resistance

The corrected local fouling resistance is determined by using the approach of Albert et al. (2011) with a local perspective, see Eq. (9). Therefore, local constrictions and the resulting local flow velocities as well as local friction coefficients based on the local layer roughness are required.

$$R_{f,loc,corr}(t,z) = \frac{1}{k_f(t,z)} - \frac{1}{k_0(z)\left(\varepsilon_{Nu,\xi}\varepsilon_{Nu,\omega}\right)_{tz}} \tag{9}$$

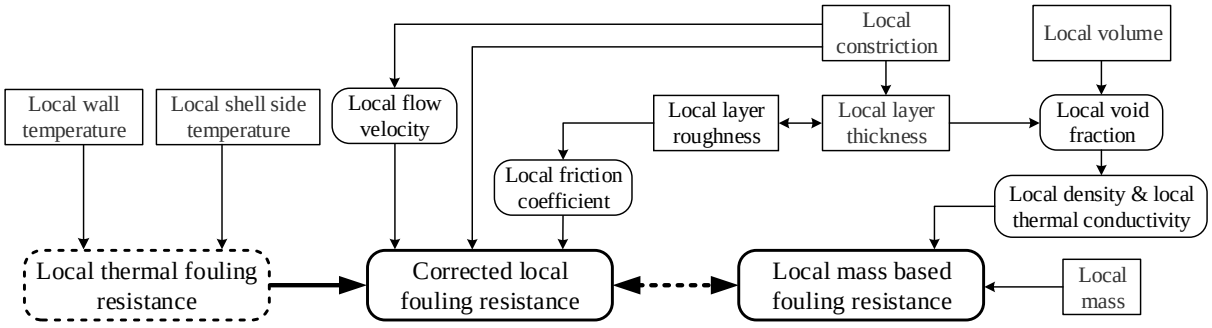

Fig. 5 Measured (rectangles) and calculated (rectangles with rounded corners) variables integrated in the modeling of local fouling resistances.

ISBN: 978-0-9984188-1-0; Published online www.heatexchanger-fouling.com

Local mass based fouling resistance

The calculation of local mass based fouling resistances is carried out by applying a local consideration of Eq. (3).

$$R_{f,mass,loc}(t,z) = \frac{m_f(t,z)}{\rho_f(t,z)\ \lambda_f(t,z)} \qquad (10)$$

Accordingly, local density and thermal conductivity are required which depend on the local void fraction of the fouling layer. The void fraction describes the part of a fouling layer which can be filled with fluid and is calculated from the local layer thickness and the local volume of the layer. Furthermore the local deposited fouling mass is required.

EXPERIMENTAL PROCEDURE

This section presents the experimental procedure to acquire the parameters displayed in rectangles in Fig. 5.

Fouling experiments with a supersaturated aqueous $CaSO_4$ solution were carried out in a test rig equipped with two double-pipe heat exchangers (HX2 and HX3, 20 x 2 x 2000 mm), shown in Fig. 6. The test rig is described in detail by Schlüter et al. (2017). The heat exchangers operate in counterflow with the salt solution entering the tube side with 42 °C inlet temperature, 1 m/s flow velocity and a $CaSO_4$ concentration of 0.027 mol/L. Hot deionized water flows through the shell side with an inlet temperature of 80 °C and a flow velocity of 0.25 m/s. The resulting Reynolds numbers are 25,500 on the tube side and 20,700 on the shell side respectively.

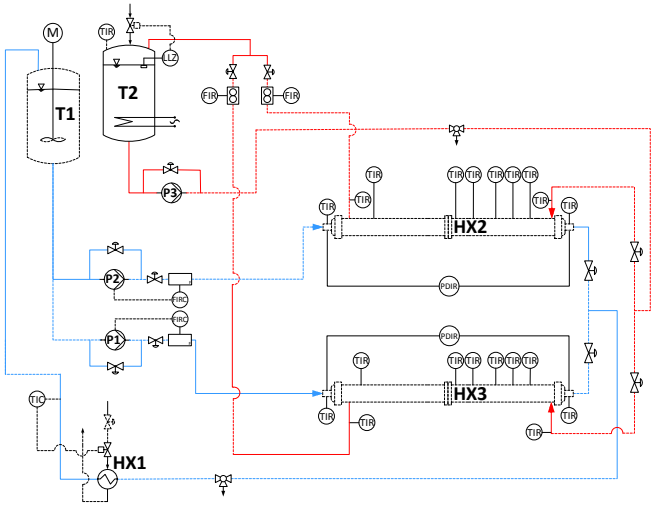

Fig. 6 Fouling test rig equipped with two double-pipe heat exchangers, a heating circuit (red) and a product circuit (blue).

One of the heat exchanger test sections is equipped with a glass fiber sensor in the wall of the inner tube and with six thermocouples in the annular gap as shown in Fig. 7. This techniques allow for determining the temperature profiles at the tube wall and of the shell side flow. With this information the local thermal fouling resistances can be calculated (Schlüter et al., 2017). The second heat exchanger is only equipped with the six thermocouples in the shell side. After a fouling test run of approximately five days the fouled inner tube of this heat exchanger is dismounted in order to investigate the axial distribution of deposit regarding its volume, mass, layer thickness and roughness. Assuming a similar fouling progress in both test sections due to identical process parameters and a similar integral pressure drop development, the glass fiber sensor provides the associated temperature profile.

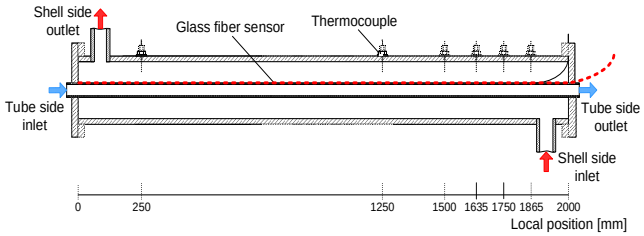

Fig. 7 Double-pipe heat exchanger equipped with thermocouples in the shell side and a glass fiber sensor in the tube wall for local temperature measurements.

Filling the tube with fouling inside incrementally with water and recording the respective water levels of a connected translucent tube by using the principle of communicating tubes provides information about the water volume displaced by deposits and therefore about the volume of the fouling layer (Schlüter, 2017). Subsequently, the tube is cut into 10 segments of 200 mm length as shown in Fig. 8.

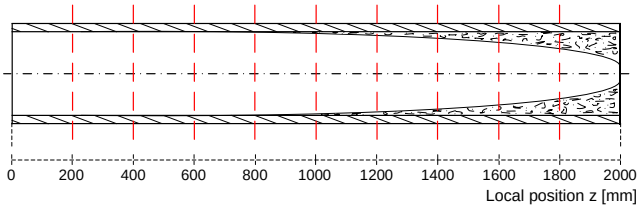

Fig. 8 Sketch of the fouled inner tube showing cuts into segments of 200 mm length to locally determine layer thickness, roughness and mass.

The local constriction as well as the layer thickness and roughness at the different axial positions can be investigated by examining photographs of each tube cross-section with a suitable image analysis software (ImageJ, Wayne Rasband, NIH). Dimensions like the tube diameter are specified and the area of different circular shapes or a freehand selection is calculated by the program.

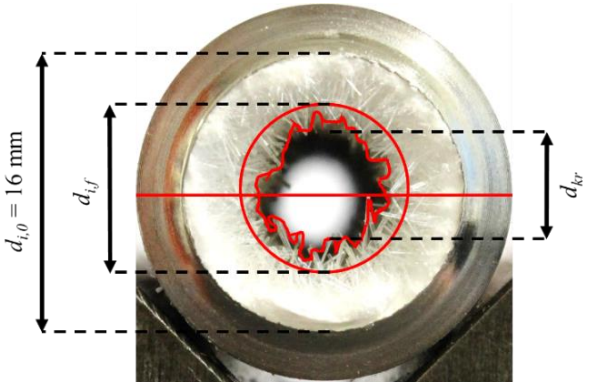

Fig. 9 Measuring the cross section of a fouled tube at z = 2 m by using image analysis software.

Fig. 9 shows an example of analyzing the cross section of a fouled tube at z = 2 m. The corresponding inner diameter

ISBN: 978-0-9984188-1-0; Published online www.heatexchanger-fouling.com

$d_{i,f}$ regarding the fouling layer thickness x_f and the diameter d_{kr} taking also the roughness height k_r into account are displayed

In addition, weighing the tube segments provides the deposited mass per segment and therefore the incremental distribution of fouling mass along the tube. After an experiment of five days the total fouling mass amounts to 3-5 % of the tube weight.

CALCULATED PARAMETERS

The experimental results are included in the calculation of the local constriction, the local flow velocity, local friction coefficients as well as local layer parameters: void fraction, thermal conductivity and density. The calculation procedure is presented in this section.

Local flow velocity and local friction coefficient

Using ImageJ on the photographs of the tube segments' cross-sections after a fouling experiment provides the free flow cross-sectional area and the corresponding inner diameter $d_{i,f}$, see Fig. 9. With an increasing constriction along the tube length and a heat exchanger operating at constant flow rate, the flow velocity will increase as well:

$$w(z) = \frac{\dot{V}}{\pi/_4 \cdot d_{i,f}(z)^2} \tag{11}$$

The approach of Nedderman and Shearer (1964) describes the friction coefficient as a function of the sand roughness k_s, see Eq. (12). The local roughness resulting from the image analysis can be used as the value for k_s assuming the similarity of the crystal layer roughness to the roughness type of sand grains (Albert, 2010). This allows for an iterative calculation of local friction factors at the end of a fouling experiment but is not allowing a time-dependent progression of local friction factors.

$$\frac{1}{\sqrt{\xi}} = 1{,}74 - 2 \cdot \log_{10}\left(\frac{k_s}{r} - \frac{10}{Re} \cdot \sqrt{\frac{8}{\xi}}\right) \tag{12}$$

Therefore, values for $\varepsilon_{Nu,\xi}$ which eliminate negative local thermal fouling resistances at any local position and at any experimental time are determined with Eq. (9). By rearranging the approach of Nunner (1956), Eq. (13), the time-dependent friction coefficient ξ_f can be calculated for each axial position as far as a local thermal fouling curve exists. The friction coefficient reaches a maximum for each local position at the most negative value of the respective fouling curve. Afterwards the friction coefficient is assumed to remain constant (Albert, 2011). The determined friction values are also applied for calculating the factor $\varepsilon_{Nu,\xi}$ with the approach of Hughmark (1975) accounting for surface roughness effects on heat transfer, Eq. (14).

$$\varepsilon_{Nu,\xi} = \frac{Nu_\xi}{Nu_0} = \left(\frac{\xi_f}{\xi_0}\right)^{1/(Pr/_2 + 1.5)} \tag{13}$$

$$Nu = \sqrt{\frac{\xi}{8}}\, Re \left[\frac{\frac{1}{0.0303 + 0.0615\, Pr^{1/2}} + \frac{1}{0.625 + 0.062\, Pr^{1/3}}}{\frac{1}{\frac{7.16}{\sqrt{\frac{\xi}{8}}Re} + + 2\sqrt{\frac{\xi}{8}}Pr}} \right]^{-1} \tag{14}$$

Local void fraction, thermal conductivity and density

The local void fraction ϵ is calculated by applying the experimental results regarding local thickness and local volume of the layer. Since the displaced water is determined segmentally the mean layer thickness within a tube segment is used. Both values are obtained from a fouled tube at its final condition after a fouling experiment. The mean local layer thickness x_f defines the cross-sectional area occupied by deposits. Multiplying this area with the length of the segment results in the total layer volume $V_{f,tot}$. Subtracting the volume of water displaced by deposits within the respective tube segment from $V_{f,tot}$ provides the volume of water $V_{H_2O,\epsilon}$ fitting in the void ϵ of the theoretically available total layer volume $V_{f,tot}$. Finally, the ratio of both parameters results in the fouling layer void fraction per tube segment:

$$\epsilon(z) = \frac{V_{H_2O,\epsilon}}{V_{f,tot}} \tag{16}$$

Since the void fraction is an incremental parameter all dependent values are calculated per tube segment as well.

The fouling layer is considered as a porous system with the local void fraction ϵ. The thermal conductivity is obtained from two alternative arrangements: solid matrix and void acting as resistances in series, see Eq. (17), and both acting in parallel, see Eq. (18) (Krischer, 1978).

$$\lambda_{f,I}(z) = \epsilon(z) \cdot \lambda_{H_2O} + (1 - \epsilon(z)) \cdot \lambda_{gyp} \tag{17}$$

$$\frac{1}{\lambda_{f,II}(z)} = \frac{\epsilon(z)}{\lambda_{H_2O}} + \frac{1-\epsilon(z)}{\lambda_{gyp}} \tag{18}$$

Since the void of the fouling layer is filled with the aqueous solution the thermal conductivity of pure water (λ_{H_2O} = 0.64 W/m K at 45 °C) is used and the thermal conductivity of gypsum (λ_{gyp} = 1.3 W/m K) is applied for the solid (Comeaux, 1987). The mean thermal conductivity of the fouling layer is calculated by averaging $\lambda_{f,I}$ and $\lambda_{f,II}$:

$$\lambda_f(z) = \frac{\lambda_{f,I}(z) + \lambda_{f,II}(z)}{2} \tag{18}$$

The density of the fouling layer is calculated with Eq. (19) when considering only the deposited salt (ρ_{gyp} = 2,320 kg/m³) with vacuum in the void fraction (Hirsch, 1997).

$$\rho_f(z) = (1 - \varepsilon(z)) \cdot \rho_{gyp} \tag{19}$$

ISBN: 978-0-9984188-1-0; Published online www.heatexchanger-fouling.com

RESULTS

Local thermal fouling resistance

Fig. 10 presents selected fouling curves obtained with the local temperature measurements using the glass fiber sensor. All curves clearly relate to the distance between the location of the measuring point and the hot water inlet of the heat exchanger. The respective local values of fouling rate and the final fouling resistance increase in direction of the hot water inlet. A decrease in heat transfer over time was detected from the axial position z = 1.38 m onwards. The fouling curve of z = 1.96 m shows the most significant enhancement of heat transfer after around one day. Therefore, a fast development of a high surface roughness can be assumed at this location. At z = 1.24 m only crystals enhancing the flow turbulence exist during the entire experimental time, resulting in a negative fouling resistance. Therefore, the fouling curve does not leave the roughness controlled period. (Schlüter, 2017)

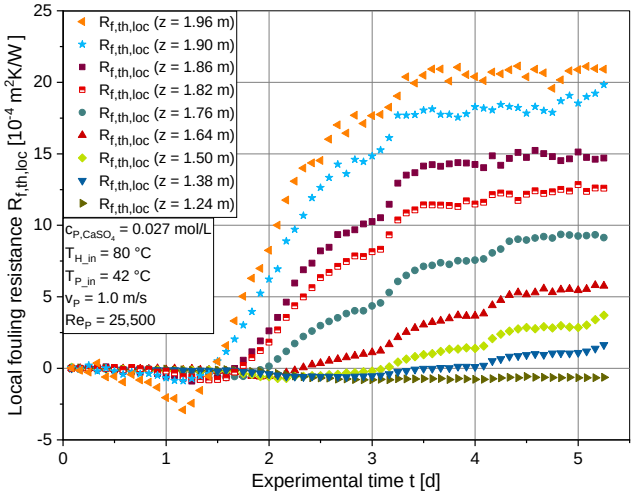

Fig. 10 Curves of local thermal fouling resistances at various local positions based on temperatures measured with the glass fiber sensor.

Corrected local fouling resistance

Fig. 11 shows recalculated local fouling resistances at z = 1.96 m in comparison to the local thermal fouling resistance with a constant heat transfer coefficient extracted from Fig. 10. In order to plot the time-dependent corrected fouling behavior only the increase in Nusselt numbers by roughness effects, Eq. (5), is considered for calculation with Eq. (9). The comprehensive study from Albert et al. (2011) attested the heat transfer correlations by Burck (1969) and Ceylan and Kelbaliyev (2003) not to be suitable for this purpose. Therefore, only corrected fouling resistances based on the approaches by Nunner (1956), Eq. (13), and Hughmark (1975), Eq. (14), are shown in Fig. 11. The negative fouling values are eliminated by taking surface roughness effects on heat transfer into account. With both applied approaches higher fouling values are calculated. Due to the procedure to calculate local and time-dependent friction coefficients, the fouling curve resulting from the empirical model of Nunner (1956) remains at zero until the local thermal fouling resistances reaches its minimum with the friction coefficient reaching its maximum. The fouling curve, calculated by considering the approach of Hughmark (1975) and utilizing the same friction coefficients, already starts to rise shortly after the experiment starts. This can be explained with a higher heat transfer rate with the rough surface to the heat transfer with the smooth surface, according to Eq. (5). Hence, higher fouling resistances are obtained in general, which was found by Albert et al. (2011) as well.

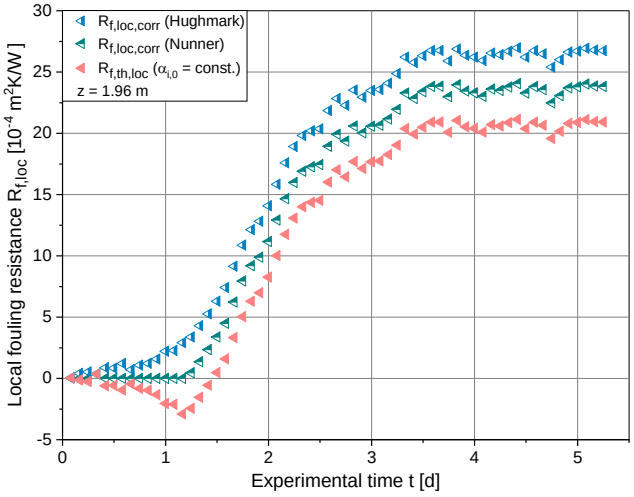

Fig. 11 Recalculated local fouling resistance at z = 1.96 m by considering heat transfer enhancing roughness effects in comparison with the measured fouling thermal resistance.

Tab.1 gives an overview over the friction coefficients used for the calculation and different calculated fouling resistances R_f^* at the end of the experiment for z = 1.96 m as well as for three additional axial positions.

Tab. 1 Friction coefficients and final fouling resistances in [m² K/W] at selected axial positions.

Local position [m]	**1.38**	**1.64**	**1.82**	**1.96**
ξ_0	0.024	0.024	0.024	0.024
ξ_{max}	0.077	0.056	0.037	0.035
$\varepsilon_{Nu,\xi,max}$ (Nunner)	1.41	1.28	1.14	1.12
$\varepsilon_{Nu,\xi,max}$ (Hughmark)	2.02	1.67	1.31	1.27
$R^*_{f,th,loc}$ ($\alpha_{i,o}$ = const.)	$1.6{\cdot}10^{-4}$	$5.8{\cdot}10^{-4}$	$12.6{\cdot}10^{-4}$	$20.9{\cdot}10^{-4}$
$R^*_{f,loc,corr}$ (Nunner)	$2.2{*}10^{-4}$	$6.4{*}10^{-4}$	$13.4{*}10^{-4}$	$23.9{*}10^{-4}$
$R^*_{f,loc,corr}$ (Hughmark)	$2.7{*}10^{-4}$	$6.8{*}10^{-4}$	$14.2{*}10^{-4}$	$26.7{*}10^{-4}$

As expected, the corrected fouling resistances are higher than the local thermal resistances at any local position. In contrast to the negative thermal fouling resistances at the respective axial positions, the values of the maximum friction coefficients ξ_{max} and therefore also of the ratio of Nusselt numbers $\varepsilon_{Nu,\xi,max}$ decrease with increasing tube length. This is owed to the temperature difference between the fluids on shell side and tube side at z = 0 m being higher by 5 K compared to z = 2 m. Therefore, the overall heat transfer

ISBN: 978-0-9984188-1-0; Published online www.heatexchanger-fouling.com

coefficients k_0 and k_f decrease with increasing tube length. Even if the difference of $1/k_f$ and $1/k_0$ gets bigger when approaching z = 2 m, the factor $\varepsilon_{Nu,\xi}$ and therefore the friction coefficient, which is needed to equalize them, decreases due to the higher absolute values of $1/k_f$ and $1/k_0$.

At the end of the fouling experiment the constriction effects on heat transfer are considered in addition for recalculating local thermal fouling resistances. The constricted inner diameter, caused by depositions distributed along the tube length, is investigated at the tube cross-sections resulting from cutting a fouled tube without the glass fiber sensor into 10 segments, as described before. The determined local constricted inner diameter and the resulting flow velocity in accordance to Eq. (11) are plotted in Fig. 12. The constricted inner diameter decreases from initially 16 mm for the clean tube at the tube inlet (z = 0 m) to a minimum of almost 10 mm at the tube outlet (z = 2 m). Accordingly, the axial development of the tube side local flow velocity is invers to the free cross-sectional area and increases from 1 m/s to 2.5 m/s.

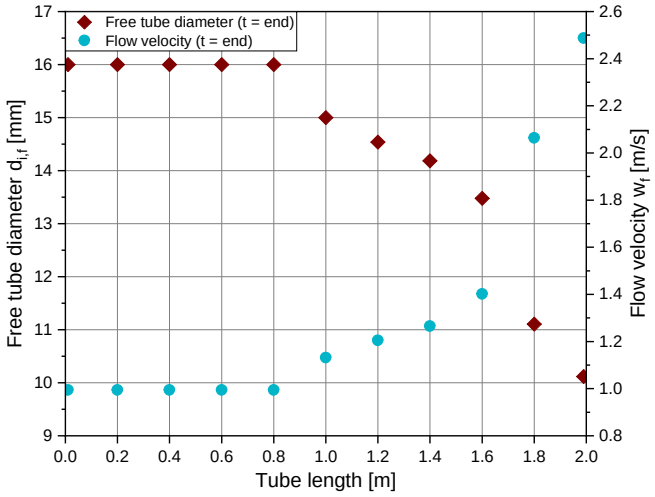

Fig. 12 Constriction of the inner diameter due to fouling and corresponding local flow velocities at the end of the fouling experiment.

In order to include the constriction effect on heat transfer in the recalculation of the final fouling resistances, presented in Tab. 1, the increase in Nusselt number is determined using the correlation of Gnielinski (1995), Eq. (7), with the local data at 1.4 m, 1.6 m, 1.8 m and 2 m. The results are presented in Tab. 2. The ratio of Nusselt numbers $\varepsilon_{Nu,\omega}$ increases with increasing axial position resulting in a raise of the corrected fouling resistances applying the correlations of Hughmark (1975) and Nunner (1956) together with the approach of Gnielinski (1995).

Overall, applying the presented heat transfer correlations for recalculating thermal fouling by taking into account roughness and constriction effects, the so far integrally regarded fouling process is now successfully transferred into a local perspective.

Tab. 2 Final corrected fouling resistances in [m² K/W] based on accounting for roughness and constriction effects.

Local position [m]	**1.38**	**1.64**	**1.82**	**1.96**
$\varepsilon_{Nu,\omega}$ (Gnielinski)	1.10	1.14	1.24	1.38
$R^*_{f,th,loc}$ ($\alpha_{i,o}$ = const.)	$1.6\cdot10^{-4}$	$5.8\cdot10^{-4}$	$12.6\cdot10^{-4}$	$20.9\cdot10^{-4}$
$R^*_{f,loc,corr}$ (Nunner + Gnielinski)	$2.4\cdot10^{-4}$	$6.6\cdot10^{-4}$	$14.6\cdot10^{-4}$	$30.6\cdot10^{-4}$
$R^*_{f,loc,corr}$ (Hughmark + Gnielinski)	$2.8\cdot10^{-4}$	$7.0\cdot10^{-4}$	$15.2\cdot10^{-4}$	$32.7\cdot10^{-4}$

Local mass based fouling resistance

Local mass based fouling resistances are calculated for each segment of the cut tube according to Eq. (10). A higher spatial resolution of the mass based fouling resistances along the tube length is not feasible at the current state since the deposited fouling mass is determined by weighing the fouled tube segments.

As shown in Fig. 5 and described by Eqs. (15-19) the experimentally determined deposited mass per area, the volume of displaced water and the fouling layer thickness are needed for calculating mass based fouling resistances as well as the calculated layer's void fraction and resulting thermal conductivity and density. Tab. 3 and Tab. 4 list the results of these parameters for ten tube segments giving an overview of the axial distribution and related changes of the local fouling layer at the end of the fouling experiment.

Tab. 3 Deposited mass, displaced water and layer thickness for ten tube segments with 200 mm length each.

Segment	**Deposited mass [g/m²]**	**Displaced water [mL]**	**Mean layer thickness [mm]**
1	28.9	0	0
2	38.5	0.2	0
3	171.3	0.1	0
4	122.9	0.2	0
5	190.8	0.4	0.25
6	304.8	0.8	0.62
7	473.0	1.4	0.82
8	785.1	2.7	1.08
9	1525.4	7.0	1.85
10	2524.9	12.8	2.69

Tab. 4 Calculated void fraction, thermal conductivity and density of the deposits inside the tube segments.

Segment	**Void fraction [-]**	**Mean thermal conductivity [W/m K]**	**Mean density [kg/m³]**
1	1	0.64	0
2	1	0.64	0
3	1	0.64	0
4	1	0.64	0
5	0.84	0.72	371.20

ISBN: 978-0-9984188-1-0; Published online www.heatexchanger-fouling.com

6	0.87	0.71	301.60
7	0.82	0.73	417.60
8	0.73	0.78	626.40
9	0.57	0.87	997.60
10	0.43	0.96	1322.40

Since no compact layer could be found within the first four tube segments (up to z = 0.8 m) the void fraction is set to 1 here. Consequently, the thermal conductivity is equal to the thermal conductivity of water and the density is set to 0 kg/m³. All further density values are in a similar range to values determined by Hirsch (1997) for different $CaSO_4$ fouling layers formed at various process parameters. In general, the thermal conductivity and density of the fouling layer increase with a decreasing void fraction.

Fig. 12 shows the local mass based fouling resistances for all tube segments plotted over the tube length in comparison to the fouling resistances listed in Tab. 2. As result of no existing values of layer thickness and layer density within the first four tube segments, no fouling resistances can be calculated with Eq. (10) and therefore were set to zero as well. The deposited masses in this segments are attributed to roughness only. The calculated values increase from $5 \cdot 10^{-4}$ m²K/W in segment 5 to $20 \cdot 10^{-4}$ m²K/W in segment 10. The mass based fouling resistances are significantly higher in comparison to the local thermal fouling resistances at 1.38 m, 1.64 m and 1.82 m. In contrast, the local fouling resistances at 1.96 m and from segment 10 are similar. Whereas taking into account roughness and constriction effects the corrected fouling resistance clearly exceeds the mass based value of segment 10. This shows that finding the link between corrected fouling resistances based on local thermal fouling resistances and the mass based fouling resistances represents a considerable challenge.

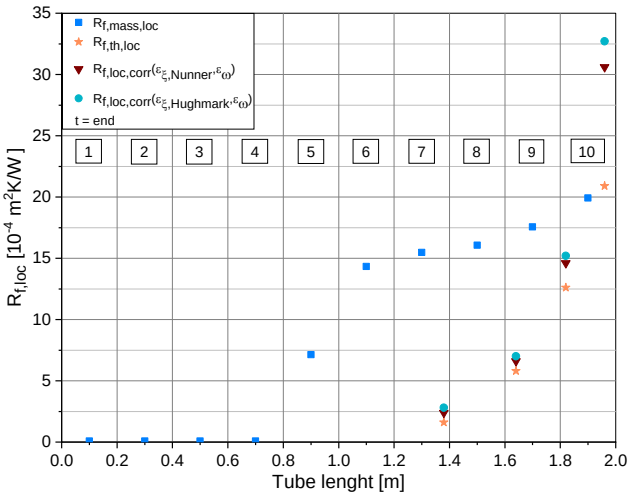

Fig. 12 Local mass based fouling resistances calculated for each tube segment compared to local thermal and local corrected fouling resistances.

CONCLUSIONS

A holistic fouling model with the aim to link the thermal and the mass based approach for calculating fouling resistances is introduced. The part of the model dealing with the local fouling resistances is presented in detail by defining all measuring categories and the resulting calculated parameters required for modeling local thermal fouling resistances, local mass based fouling resistances and the corrected local fouling resistance. The latter is a recalculated form of the local thermal fouling resistance accounting for heat transfer enhancing effects by surface roughness and constriction.

In order to provide data for modeling the local fouling resistances, fouling experiments in a double-pipe heat exchanger are conducted under constant process conditions. Crystallization fouling of an aqueous $CaSO_4$ solution is examined with a local perspective. The fouling progress is investigated locally by measuring local temperatures with a glass fiber sensor along the heat exchanger. This allows for modeling time-dependent local thermal fouling resistances. Further experimental methods, e.g. cutting the fouled tube into segments, provide data regarding the local fouling volume, mass, thickness and roughness per tube segment. With this parameters the fouling layer properties void fraction, thermal conductivity and density are calculated. All experimental and theoretical approaches are merged into the model for the determination of the different local fouling resistances.

Negative fouling resistances in the roughness controlled phase of the local thermal fouling resistances are eliminated by accounting for heat transfer enhancement through roughness. Consequently, the final fouling values at the end of the experiment increase. An additional consideration of constriction effects on heat transfer at the end of the experiment raises the effective fouling resistances even more. Comparing the values obtained by the thermal, mass based and the corrected approach shows significant differences. The goal of ongoing work is to correlate corrected and mass based fouling resistances. For this reason, an estimation of the time-dependent local constriction effects will be necessary. In addition, an additional approach to determine the time-dependent local friction coefficients needs to be implemented in order to overcome the discrepancies between negative local thermal fouling resistances and the corresponding maximum friction coefficients.

NOMENCLATURE

A	area, m²
c	concentration, mol/L
d	tube diameter, m
k	overall heat transfer coefficient, W/(m²K)
k_r	roughness height, m
k_s	sand roughness, m
m_f	deposited mass per area, kg/m²
Nu	Nusselt number, -
Pr	Prandtl number, -
Re	Reynolds number, -
r	tube radius, m
R_f	fouling resistance, m²K/W
t	experimental time, d
T	temperature, °C
V	volume, m³
$\dot{V}$	volume flow, m³/h

ISBN: 978-0-9984188-1-0; Published online www.heatexchanger-fouling.com

w	flow velocity, m/s
x_f	fouling layer thickness, m
z	axial position, m

Greek letters

α	heat transfer coefficient, W/(m²K)
Δp	pressure drop, Pa
ϵ	void fraction, -
ε_{Nu}	ratio of Nusselt numbers, -
λ	thermal conductivity, W/(mK)
ξ	friction factor, -
ρ	density, kg/m³

Subscripts

0	clean surface
b	bulk
$corr$	corrected
f	fouling
gyp	gypsum
H	water stream
H_20	water
i	inner
in	inlet
ind	induction phase
ini	initiation phase
loc	local
m	mean
$mass$	mass based
max	maximum
tot	total
ϵ	void
ξ	roughness effects
ω	constriction effects
P	product stream
th	thermal
w	wall

Acronyms

$CaSO_4$	calcium sulphate
HX2	double-pipe heat exchanger test section 2
HX3	double-pipe heat exchanger test section 3

REFERENCES

Albert, F., 2010, Grenzflächeneffekte bei der kristallinen Belagbildung auf wärmeübertragenden Flächen, *Dissertation*, Technische Universität Braunschweig, Germany

Albert, F., Augustin, W., and Scholl, S., 2011, Roughness and constriction effects in crystallization fouling, *Chem. Eng. Sci.*, Vol. 66 (3), pp. 499-509.

Al-Janabi, A, Malayeri, M.R., and Müller-Steinhagen, H, 2009, Experimental investigation of crystallization fouling on grooved stainless steel surfaces during convective heat transfer, *Heat Transfer Eng.*, Vol 30 (10-11), pp. 832-839.

Augustin, W., and Bohnet, M, 1995, Influence of the ratio of free hydrogen ions on crystallization fouling, *Chem. Eng. Process.*, Vol. 34 (2), pp. 79-85.

Bohnet, M., and Augustin, W, 1993, Effect of surface structure and pH-value on fouling behaviour of heat exchangers, in J. S. Lee et al.: Transport Phenomena in Thermal Engineering, Begell House, New York, pp. 884-889.

Burck, E., 1969, Der Einfluss der Prandtlzahl auf den Wärmeübergang und Druckverlust künstlich aufgerauter Strömungskanäle, *Heat Mass Transfer*, Vol. 2, pp. 87-98.

Ceylan, K., and Kelbaliyev, G., 2003, The roughness effects on friction and heat transfer in the fully developed turbulent flow in pipes, *Appl. Therm. Eng.*, Vol. 23 (5), pp. 557-570.

Comeaux, R.V., 1978, Calcium sulphate anhydrite scaling of water-cooled exchangers, *Material Performance*, Vol. 17 (11), pp. 9-21.

Fahiminia, F., Watkinson, A.P., and Epstein, N., 2007, Early events in the precipitation fouling of calcium sulphate dihydrate under sensible heating conditions, *Can. J. Chem. Eng.*, Vol. 85 (5), pp. 679–691.

Gnielinski, V., 1995, Ein neues Berechnungsverfahren für die Wärmeübertragung im Übergangsbereich zwischen laminarer und turbulenter Rohrströmung, *Forsch. Ing.-Wes.*, Vol. 61 (9), pp. 240-249.

Goedecke, R., Drögemüller, P., Augustin, W., and Scholl, S., 2016, Experiments on integral and local crystallization fouling resistances in a double-pipe heat exchanger with wire matrix inserts, *Heat Transfer Eng.*, Vol. 37 (1), pp. 24-31.

Helalizadeh, H., Müller-Steinhagen, H., and Jamialahmadi, M., 2000, Mixed salt crystallization fouling, *Chem. Eng. Process*, Vol. 39 (1), pp. 29-43.

Hirsch, H., 1997, Scher- und Haftfestigkeit kristalliner Foulingschichten auf wärmeübertragenden Flächen, *Dissertation*, Technische Universität Braunschweig, Germany

Hughmark, G.A., 1975, Heat, mass, and momentum transport with turbulent flow in smooth and rough pipes, *AIChE J.*, Vol. 21 (5), pp. 1033-1035.

Kern, D.Q., and Seaton, R.A., 1959, A theoretical analysis of thermal surface fouling, *British Chem. Eng.*, Vol. 4, pp. 258-262.

Krause, S., 1993, Fouling of heat transfer surfaces by crystallization and sedimentation, *Int. Chem. Eng.*, Vol. 33 (3), pp. 335-401.

Krischer, O., 1978, Die wissenschaftlichen Grundlagen der Trocknungstechnik, Springer-Verlag Berlin Heidelberg

Müller-Steinhagen, H., 2011, Heat Transfer Fouling: 50 years after the Kern and Seaton model, *Heat Transfer Eng.*, Vol 32 (1), pp. 1-13.

Müller-Steinhagen, H., Zhao, Q., Helali-Zadeh, A., and Ren, X.-G., 2000, The effect of surface properties on $CaSO_4$ scale formation during convective heat transfer and subcooled flow boiling, *Can. J. Chem. Eng.*, Vol. 78 (1), pp. 12-20.

Nedderman, R.M., and Shearer, C.J., 1964, Correlations for the friction factor and velocity profile in the transition region for flow in sand-roughened pipes, *Chem. Eng. Sci.*, Vol. 19 (6), pp. 423-425.

ISBN: 978-0-9984188-1-0; Published online www.heatexchanger-fouling.com

Nunner, W., 1956, Wärmeübergang und Druckabfall in rauen Rohren, *VDI Forschungsheft*, Vol. 455, VDI-Verlag, Düsseldorf

Pääkkönen, T.M., Riihimäki, M., Simonson, C.J., Muurinen, E., and Keiski, R.L., 2012, Crystallization fouling of $CaCO_3$ – Analysis of experimental thermal resistance and its uncertainty, *Int. J. Heat Mass Transfer*, Vol. 55 (23-24), pp. 6927-6937.

Schlüter, F., Schnöing, L., Zettler, H., Augustin, W., and Scholl, S., 2017, Measuring local crystallization fouling in a double-pipe heat exchanger, *Proc. Int. Conf. Heat Exchanger Fouling and Cleaning 2017*, Aranjuez, Spain, pp. 75-82.

Schoenitz, M., Grundemann, L., Augustin, W., and Scholl, S., 2015, Fouling in microstructured devices: a review, *Chem. Commun.*, Vol. 51 (39), pp. 8213-8228.

Zettler, H.U., Weiss, M., Zhao, Q., and Müller-Steinhagen, H., 2005, Influence of surface properties and characteristics on fouling in plate heat exchangers, *Heat Transfer Eng.*, Vol. 26 (2), pp. 3-17.

ISBN: 978-0-9984188-1-0; Published online www.heatexchanger-fouling.com